ANNUAL REVIEWS

*Annual Review of Chemical and Biomolecular Engineering*

# Positron Emission Particle Tracking of Granular Flows

C.R.K. Windows-Yule,[1] J.P.K. Seville,[1] A. Ingram,[1] and D.J. Parker[2]

[1]School of Chemical Engineering, University of Birmingham, Edgbaston, Birmingham B15 2TT, United Kingdom; email: c.r.windows-yule@bham.ac.uk

[2]School of Physics and Astronomy, University of Birmingham, Edgbaston, Birmingham B15 2TT, United Kingdom



Annu. Rev. Chem. Biomol. Eng. 2020. 11:367–96

First published as a Review in Advance on March 30, 2020

The *Annual Review of Chemical and Biomolecular Engineering* is online at chembioeng.annualreviews.org

https://doi.org/10.1146/annurev-chembioeng-011620-120633



## Keywords

positron emission particle tracking, PEPT, granular, powder, particulate, flow, imaging, dynamics

## Abstract

Positron emission particle tracking (PEPT) is a noninvasive technique capable of imaging the three-dimensional dynamics of a wide variety of powders, particles, grains, and/or fluids. The PEPT technique can track the motion of particles with high temporal and spatial resolution and can be used to study various phenomena in systems spanning a broad range of scales, geometries, and physical states. We provide an introduction to the PEPT technique, an overview of its fundamental principles and operation, and a brief review of its application to a diverse range of scientific and industrial systems.

## 1. INTRODUCTION

Positron emission particle tracking (PEPT) is a powerful technique capable of imaging the three-dimensional motion of powder, granular, multiphase, and fluid flows with submillimeter accuracy and submillisecond temporal resolution. Particles are tracked using high-energy (511-keV) $\gamma$ photons, meaning that their motion can be followed even deep within the interior of large, dense, optically opaque systems. This makes PEPT a valuable technique for the study of diverse scientific and industrial processes and phenomena.

Although PEPT is a well-established technique, having first been developed in the 1980s at the University of Birmingham (1–4), the methods, tracers, algorithms, software, and hardware used to perform PEPT have been (and continue to be) developed and improved continuously over the past three decades. In this review, we provide an overview of these developments, beginning in the next section with an introduction to the fundamentals of the technique, and ending with an overview of, and reference guide to, the various studies that have been performed using PEPT across a diverse range of systems and how they have advanced our knowledge and understanding of granular media.

## 2. THE PEPT TECHNIQUE: TRACKING

### 2.1. Fundamental Principles

In order to track the motion of a particle through a granular system, said particle must first be radioactively labeled with a positron-emitting radioisotope.[1] The particle chosen as a tracer is typically physically identical to others in the system to be investigated, even after the labeling process, meaning that PEPT can easily be used for noninvasive imaging.

The short mean range of positrons in a typical granular medium [~0.5 mm for a material with a bulk density of 1,500 kg/m$^3$ (5, 6)] means that they will rapidly annihilate with electrons within or in the immediate vicinity of the tracer particle, releasing a pair of 511-keV photons whose trajectories—due to conservation of momentum—are collinear (to within 0.5°) and antiparallel (**Figure 1*a***). If the system containing the tracer particle is placed within the field of view of a

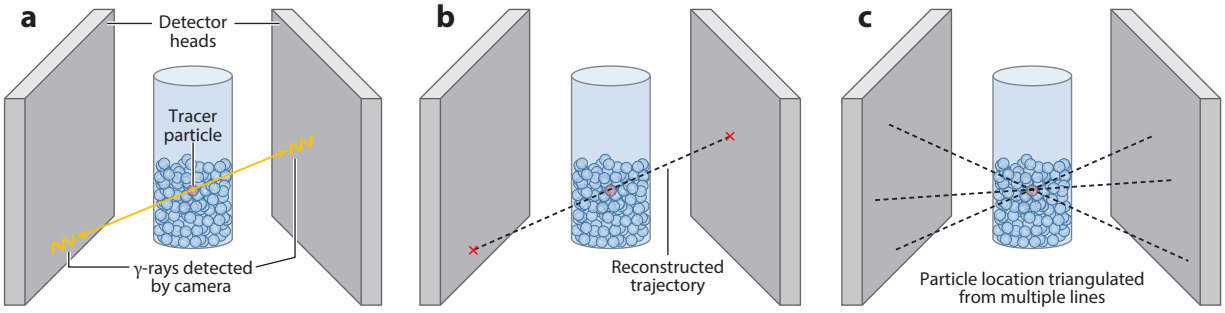


**Figure 1**

How positron emission particle tracking (PEPT) locates a single tracer particle in a granular system. If an active tracer particle (depicted in red for clarity, though in reality identical to all others of its species) emits a pair of back-to-back $\gamma$ photons (*a*) that are simultaneously recorded by the detectors of the positron camera, their trajectory can be reconstructed algorithmically (*b*). By finding the point of intersection of several such lines (*c*), one can determine the position of the tracer's center.

[1]The precise ways in which a particle may be labeled, and the specific isotopes commonly used, are discussed in detail in Section 4.

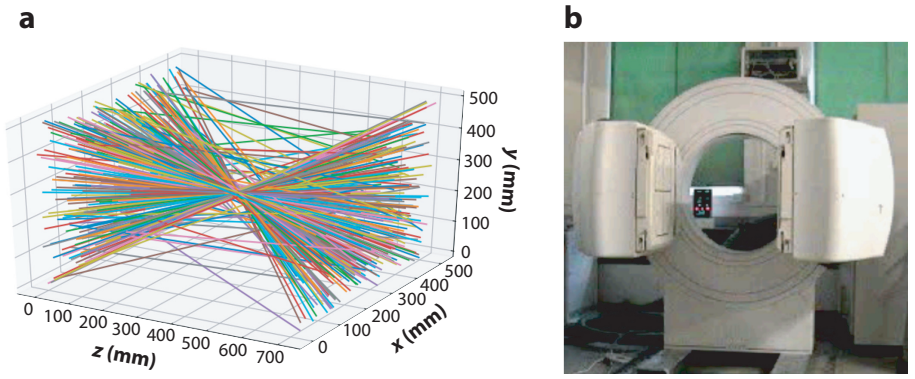


**Figure 2**

Example of a set of 400 apparent lines of response (*a*) belonging to a single particle placed between the heads of an ADAC dual-headed $\gamma$ camera (*b*).

suitable detector system[2]—for example, the two-headed positron camera schematically depicted in **Figure 1**—the positions at which emitted $\gamma$ photons hit the detector are recorded.

The detection of any two photons within a predefined resolving time (typically of the order of nanoseconds) is considered a coincidence event, meaning that it is possible that the two photons were emitted simultaneously from the same positron annihilation. If the detected photons do indeed belong to such a pair, the recorded positions of the photons' interactions with the detectors can be used to recreate the collinear trajectory followed (**Figure 1*b***). Using several such lines of response (LoRs) belonging to multiple annihilation events, one can triangulate the position of the tracer in three-dimensional space (**Figure 1*c***).

Of course, the picture presented in **Figure 1** is a gross oversimplification. A set of LoRs corresponding to real experimental data is shown in **Figure 2**, illustrating the clear divergence from the idealized picture presented in **Figure 1**. In reality, on the order of tens, or more commonly hundreds, of LoRs are required in order to determine accurately the location of a particle's center. This is because $\gamma$-ray pairs may be emitted from anywhere within—or, as mentioned above, slightly outside—the tracer's volume.

In addition, any PEPT detector system will be subject to false coincidences, that is, pairs of unrelated photons hitting opposing detectors within the system's resolving time. These may take two main forms: random coincidences caused by entirely unrelated photons (**Figure 3*a*,*b***) and scattered coincidences relating to photon pairs emitted from a real positron annihilation event, but for which one or both members deviate from their collinear trajectory due to interactions with the surrounding medium (**Figure 3*c***). **Figure 2** shows a set of LoRs acquired from real experimental data, illustrating the extent of these issues.

The combination of the above issues means that, in order to locate precisely the centroid of a particle, we must both (*a*) discard any false coincidences and (*b*) find a way in which to determine the particle's true center from the many annihilation events scattered throughout its volume. The algorithms used to undertake this process are discussed in detail in Sections 2.2.1–2.2.2.

As the location of a tracer requires only a finite number of LoRs, a suitably active tracer may be located multiple times per second. For example, by using 100 LoRs per location, a particle with activity 1 MBq, for which 10% of the $\gamma$-ray pairs emitted are detected by the camera (i.e., an event rate of 100 kHz), may be located 1,000 times per second. As such, PEPT can be used to determine

[2]Greater detail regarding the detector systems used in PEPT imaging can be found in Section 3.

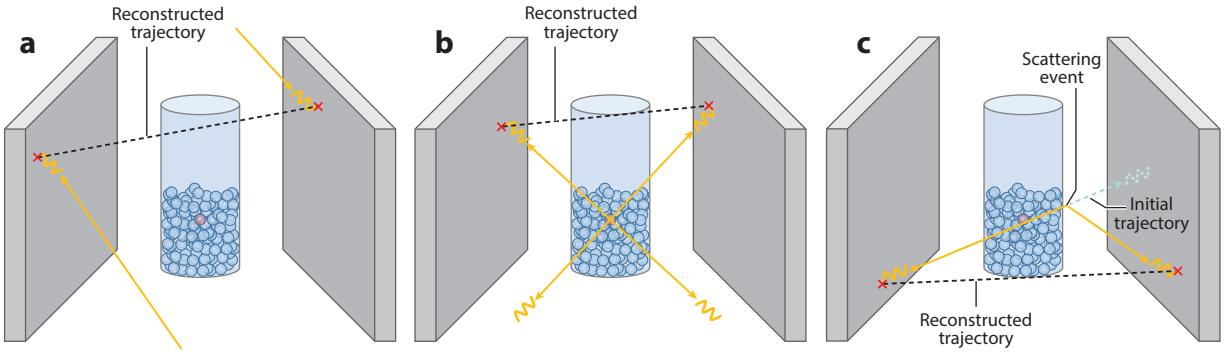


**Figure 3**

Examples of false coincidences. (*a*) A random coincidence caused by two background photons randomly interacting with the opposing detectors within the system's resolving time. (*b*) A random coincidence caused by photons from two separate annihilation events being detected within the resolving time. (*c*) A scattered coincidence, whereby one member of a photon pair is scattered, creating a false line of response.

not only the location of particles but also their trajectories, their pseudoinstantaneous velocities, and a host of other data, as discussed in Section 5.

As one may intuitively expect, the accuracy with which one may locate a particle increases with the number of LoRs used (7). Indeed, using some algorithms, a particle can be tracked with an arbitrarily high degree of accuracy as the number of LoRs tends toward infinity. However, increasing the number of LoRs per location—assuming a finite, approximately constant event rate—will inherently reduce the maximum number of locations per unit time. As such, when applying PEPT, one must typically strike a balance between spatial and temporal resolution. The number of LoRs per location can be optimized for a given experiment. For example, for a slow-moving tracer, a larger number of events per location may be used to maximize spatial resolution, as temporal resolution is not a concern. Conversely, for a fast-moving tracer, it may be preferable to use a smaller number of events and hence a greater number of locations per second. To provide a simple, quantitative example, using the University of Birmingham's ADAC camera (**Figure 2**), a particle traveling at 1 m/s may be located to within an accuracy of 1 mm 1,000 times per second. With more modern hardware, however, these statistics can be significantly exceeded, potentially by several orders of magnitude—a matter discussed further at the end of this review.

## 2.2. Algorithms

As is clear from the previous section, the accurate determination of a particle's centroid is not a trivial task. In this section, we provide a brief overview of a number of common algorithms that may be used to extract this information from raw PEPT data such as those shown in **Figure 2**.

**2.2.1. The Birmingham method.** The original, and still the most widely used, PEPT algorithm was developed at the University of Birmingham in the early 1990s (4, 8). It works by iteratively removing the least accurate LoRs from a given sample until only those closest to the true centroid remain.

More specifically, the algorithm operates as follows:

1. A sample comprising a number, $N_e$, of events (LoRs) from which to determine a location is chosen.
2. The minimum distance point (MDP)—that is, the point in space from which the sum of the squared distances to all $N_e$ is minimized—is calculated for the current sample (**Figure 4*a***).

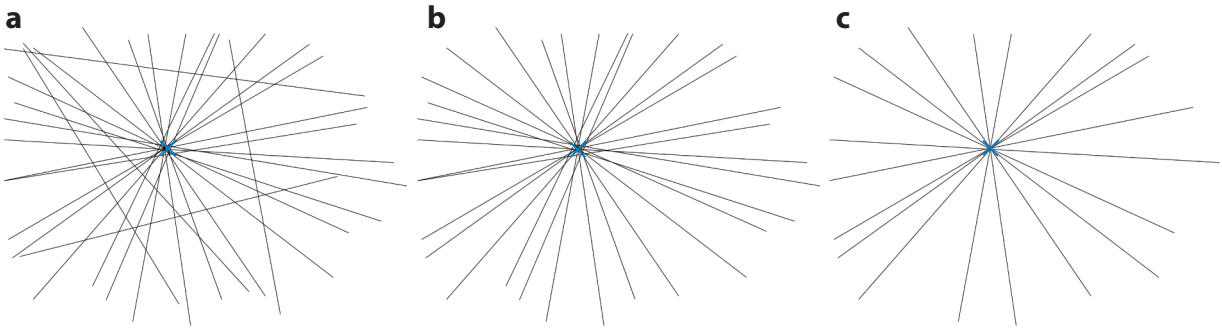


**Figure 4**

The Birmingham method. (*a*) The algorithm determines the minimum distance point (MDP) of a sample of lines of response (LoRs). (*b*) Those LoRs lying furthest from the MDP are removed from the sample, and the MDP is recalculated using the remaining events. (*c*) The LoRs lying furthest from the recalculated MDP are removed, and this process is repeated until—assuming a suitably chosen value of *f*, the final fraction of events to retain—only accurate LoRs remain, allowing the particle's centroid to be precisely located.

3. The $N_d$ LoRs lying furthest from the current MDP are discarded (**Figure 4*b***).
4. A new MDP is computed for the remaining LoRs.
5. Steps 3 and 4 are repeated until only a predetermined fraction *f* of the original events remain (**Figure 4*c***).
6. The MDP of the remaining $fN$ points is taken as the particle centroid.
7. A new sample is chosen, and steps 1–6 are repeated for the next time step.

In the above process, we consider only the location of a single tracer. However, the Birmingham method can also be adapted for the case of multiple tracers (9, 10) using the following process:

1. The first (typically most active[3]) particle is located by following steps 1–7 outlined above.
2. A new data set is created using only events discarded in the previous step.
3. The next particle in the system is then located by following steps 1–7 for the new data set.
4. Steps 2 and 3 are repeated until all tracers within the system are found.

Note that the above process requires a priori knowledge of the total number of tracers within the system. As such, this method is not recommended for systems in which, for example, particles may move into and out of the field of view of the positron camera used.

The Birmingham multiple-particle tracking method is capable of tracking up to four individual tracers to within a distance of twice the spatial resolution of the camera used for imaging. Further details regarding the Birmingham method for both single and multiple tracers may be found in Reference 4 and References 9 and 10, respectively.

**2.2.2. The line density method.** The line density method (11), developed at the University of Cape Town, adopts an entirely different approach from the Birmingham method and can be briefly described as follows:

1. The experimental volume is subdivided into a three-dimensional Cartesian grid.
2. For a given sample, the number of LoRs passing through each cell is recorded (**Figure 5**). The tracer is assumed to lie within the voxel through which the largest number of LoRs pass.

[3]Note that this method of multiple-particle location does not require the use of tracers with differing activities, though the presence of differing activities makes the identification of individual particles in the subsequent tracking process considerably simpler.

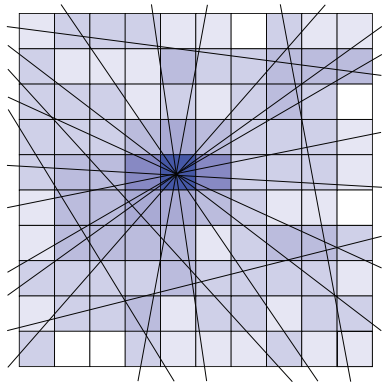

**Figure 5**

A two-dimensional cross section of the three-dimensional mesh of voxels recording local line density. The tracer is assumed to lie within the bounds of the voxel with the highest line density, specifically that through which the largest number of lines of response pass.

3. In order to determine the particle centroid with subvoxel accuracy, for all three Cartesian coordinates, a Gaussian is fitted to a histogram corresponding to the line densities of the abovementioned voxel and a row of its neighbors lying along the relevant Cartesian axis.
4. The coordinates of the particle's center are taken as the centroids of the three fitted Gaussians.

The line density method has been used successfully to track up to eight particles simultaneously. However, like the Birmingham method, it requires a priori knowledge of the number of tracers in the system.

**2.2.3. The clustering method.** The clustering method, developed at the University of Tennessee, Knoxville, begins—like the standard line density method described above—by creating a three-dimensional array of line density values. Gaussian-means clustering (12), an adaptation of $k$-means clustering (13), is then used to identify the centroid(s) of the tracer(s) to be located.

A step-by-step overview of the process can be given as follows:

1. The experimental volume is subdivided into a three-dimensional Cartesian grid.
2. For a given sample, the number of LoRs passing through each cell is recorded.
3. The algorithm first considers the case of a single cluster ($k = 1$) and then calculates a universal centroid for all data within the grid.
4. The algorithm attempts to fit a Gaussian form to the cluster currently under consideration.
5. The quality of the fit is assessed, for example, via an Anderson–Darling test (14):
   (a) If the current cluster passes the test, it is accepted as a cluster and its centroid is taken as a tracer location.
   (b) If the current cluster fails the test, the cluster is split into two, and steps 4 and 5 are repeated for $k_{\text{new}} = k_{\text{old}} + 1$.

The above process continues until all viable clusters are found. This method hypothetically requires no a priori knowledge of the number of particles in the system, although it does require data to be prefiltered to ensure that there exists at least one tracer within the field of view.

**2.2.4. Recently developed techniques.** In the preceding sections, we have provided a relatively detailed explanation of some well-established PEPT algorithms. In the final part of this section, we provide a brief overview of more recently developed algorithms, which may one day become the new standard.

***2.2.4.1. The feature point identification method.*** Like the two above-described methods, the feature point identification (FPI) technique also utilizes line density (15). In this method, however, the values of line density assigned to each voxel are converted to gray values, and standard image analysis techniques, specifically FPI (16, 17), are applied to the resultant data. The technique is capable of locating up to 100 particles, though the location error increases as the square root of the number of tracers used.

***2.2.4.2. Voronoi-based multiple-particle tracking.*** The Voronoi-based multiple-particle tracking (VMPT) method (18) operates by discretizing detected LoRs and using these discrete points as seed points for a Voronoi tessellation (19). As one can expect the density of seed points to increase in the vicinity of a tracer, the size of the local Voronoi regions near a tracer can therefore be expected to decrease. The location of the tracer is then determined by discarding outlier data—corresponding to Voronoi cells with areas significantly larger than the mean—and clustering the remaining data points. The geometric center of these clusters is taken as the tracer location. This method can track at least 20 particles.

***2.2.4.3. PEPT using machine learning.*** PEPT using machine learning (PEPT-ML) (20, 21), the most recently developed PEPT algorithm, operates by determining the MDP (or cutpoint) between every pair of LoRs detected by a scanner. Cutting-edge machine learning techniques—specifically the HDBSCAN algorithm (22)—are then used to identify clusters autonomously on the basis of both the Euclidean distance separating local cutpoints and the density (or sparsity) of their nearest neighbors. The method is capable of tracking at least 128 individual tracers simultaneously, with no observable loss of accuracy in comparison to the single-particle case.

## 3. DETECTOR SYSTEMS

In Section 2, we have introduced the basic concept of PEPT imaging using a highly simplified depiction of a dual-headed positron camera. In this section, we discuss the construction and operation of such positron cameras in greater detail, and introduce the various other main forms of detector that may be used to perform PEPT.

### 3.1. Fundamentals of Positron Imaging Systems

As is clear from Section 2, the main function of a detector in PEPT imaging is to record the spatial locations of high-energy photons such that they may be used—as described in Section 2.1—to reconstruct LoRs and hence triangulate the positions of positron-emitting tracers.

A positron camera may—as discussed further below—take many forms, but in most cases it consists of an array of multiple, individual detectors, each capable of detecting the interaction of an incident $\gamma$ photon. If the spatial positions of these detectors are known, then, by definition, the coordinates of any photon interacting with a given detector can be estimated; the precision of this estimation depends on the size, geometry, and other characteristics of the detector. If two photons interact within the predefined resolving time (typically 0.5–10 ns) with two separate detectors placed at differing spatial positions, an LoR between the two can be mathematically determined

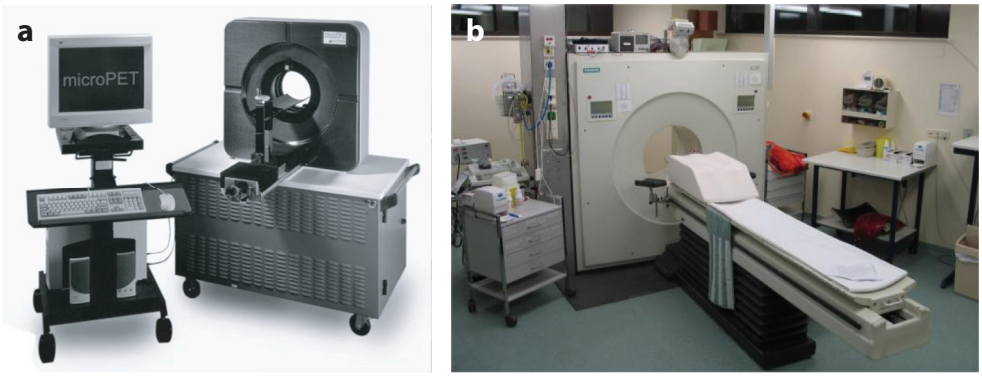


**Figure 6**

(*a*) A Concorde Microsystems microPET P4 scanner as used in positron emission particle tracking (PEPT) research performed at the University of Tennessee, Knoxville. (*b*) A Siemens ECAT EXACT3D camera as used by the University of Cape Town.

on the basis of a suitable set of assumptions concerning the most likely interaction points of the photons within the two detectors' volumes. As such, with enough detectors, suitably arranged in space, one may acquire multiple LoRs from which a tracer particle's spatial coordinates may be determined, as outlined in Section 2.

## 3.2. Static Cameras

The most common detector arrangements are that of two flat, parallel detectors (such as the dual-headed ADAC camera pictured in **Figure 2**) and that of the ring geometry (e.g., **Figure 6**).

The first positron camera used to perform PEPT comprised a pair of multiwire proportional chambers (MWPCs). MWPCs consist, as their name implies, of a series of thin wires, held at a high potential in a gas-filled tube. When ionizing radiation ionizes the gas in the tube, the free electrons released are attracted to the nearest wires, causing a localized cascade of ionization, and hence a detectable pulse in those wires. By cross-referencing the magnitudes of the pulses felt in different wires, whose positions are precisely known, one can determine the region of the detector in which the original ionization event must have occurred. Each MWPC used in the original Birmingham PEPT experiments had a sensitive area of size 600 × 300 $mm^2$ and possessed a spatial resolution of approximately 8 mm (1, 23, 24). Cameras of this form are, however, severely limited by their low efficiency and hence low data-logging rate (~3,000 Hz) (24), and as a result they are no longer used for PEPT imaging.

At the turn of the new millennium, the original Birmingham camera was replaced with a dual-headed ADAC Forté positron camera (**Figure 2**), which again used a parallel two-detector geometry but replaced the MWPC detectors with thallium-doped sodium iodide [NaI(Tl)] detectors, offering a significant improvement in both data rate and quality (7). Each detector head comprises a single NaI(Tl) crystal of area 590 × 470 $mm^2$ and thickness 16 mm that is optically coupled to an array of 55 photomultiplier (PM) tubes. When a $\gamma$ photon interacts with the sodium iodide scintillator, its energy is converted into a number of lower-energy photons falling within the optical spectrum. These photons may then enter a PM tube where, due to the photoelectric effect, they stimulate the emission of electrons; the weak current thus produced is amplified until it represents a measurable electrical signal, whose amplitude is representative of the amount of energy deposited into the PM tube. As the single NaI(Tl) crystal is coupled to a two-dimensional

array of PM tubes, the signals measured by adjacent detectors may be used to determine the centroid of the scintillation in the two-dimensional plane of the detector. This detector array offers a raw spatial resolution of approximately 6 mm[4] and a data rate of up to 100 kHz.

The PEPT facilities in both South Africa and the United States use positron cameras with ring geometries (**Figure 6**), though with notably differing properties. Cape Town's ECAT EXACT3D camera consists of 48 82-cm-diameter rings of bismuth germanate (BGO) detector elements, which—other than the choice of scintillator—operate exactly as the NaI(Tl) detectors described above (25, 26). This system offers a detector resolution of approximately 4 mm (25, 26). The system used by the University of Tennessee, Knoxville (27), possesses a smaller (261-mm-diameter) ring comprising 168 lutetium oxyorthosilicate detectors but offers a higher (1.75-mm) spatial resolution (28).

Ring detectors operate using the same general methodology as described for parallel plates, above. The main differences between the two systems are that (*a*) ring detectors offer a 360° field of view, and hence may hypothetically detect a greater percentage of emitted photons, and (*b*) whereas parallel-plate detectors utilize single scintillator blocks, ring detectors must use smaller, individual blocks. This quantization may act to compromise the spatial resolution of the detectors to an extent.

### 3.3. Modular Cameras

All of the systems discussed in the preceding section possess a largely fixed geometry[5] and—with the possible exception of Knoxville's microPET scanner—are not realistically portable. These limitations can prove problematic, as many industrial systems that may usefully be imaged using PEPT possess geometries not easily accommodated by such scanners. The lack of portability also limits the use of these systems in situ. Such in situ imaging can be highly useful, for example, as a means of monitoring a single part of a continuous process that cannot easily be downsized into a laboratory-scale system.

In order to address the above issues, researchers at the University of Birmingham have developed portable modular positron cameras (29, 30) whose geometries may be altered to accommodate an almost limitless range of system geometries. The systems are created using BGO detector blocks harvested from Siemens ECAT series scanners. Individual buckets or modules (**Figure 7**), each comprising four detector blocks, can be arranged in a desired geometry. Each of the $N_m$ modules used is in coincidence with the remaining $N_m - 1$ and—unlike in normal ring detectors, where only coincidences in the same or adjacent rings are counted—coincidences in the modular camera are accepted between any pair of modules.

The modular camera system is highly flexible, yet in theory maintains the same intrinsic spatial and temporal resolution as the scanners from which the modules are obtained. The ultimate accuracy of the systems is, however, limited by certain practical factors. First, and most notably, in order to convert measured coincidences into accurate LoRs (and hence precise particle locations), the positions of all detector blocks must be precisely known, as any inaccuracies in placement can introduce potentially serious systematic errors. Second, variations in detector sensitivity due

[4]Note that the spatial resolution of the cameras themselves does not directly equate to the accuracy with which a particle may be located, the latter typically being significantly higher due to the implementation of the algorithms described in Section 2.2. For example, the cameras described here, despite having an inherent spatial resolution of 6 mm, may be used to detect a tracer moving at 1 m/s to within 0.5 mm 250 times per second. This resolution may be refined even further for slower-moving particles and/or lower acquisition rates.

[5]Note that Birmingham's positron camera possesses some flexibility, in that it may be rotated about the horizontal $x$ axis and its dimensionality in the $z$ direction may be varied within a predefined (0–800-mm) range; however, the detector's maximal $500 \times 500 \times 800$ mm$^3$ cuboidal field of view remains a limitation.

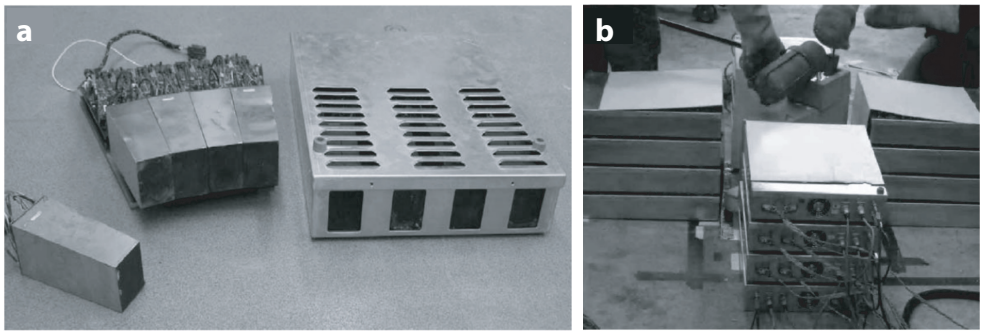


**Figure 7**

(*a*) (*left to right*) A detector block, detector bucket, and detector module. (*b*) A modular camera array, consisting of 16 individual modules, used to study the casting of molten aluminium.

to gaps between detectors (which, depending on the chosen detector arrangement, may be large and/or uneven) must be accounted for. Nonetheless, the modular system facilitates PEPT studies in new environments, and of systems otherwise impossible to image, and has been demonstrated to operate at data rates >1 kHz and with submillimeter location accuracy.

## 4. TRACERS

### 4.1. Requirements of a PEPT Tracer

For a particle to make a successful PEPT tracer, it must possess certain fundamental properties. First, and most obviously, it must emit positrons and (hence) back-to-back $\gamma$ photons; as is clear from the description of the technique in Section 2, the emission of photons with collinear trajectories is crucial to the ability of the technique to locate particles.

Second, the tracer used should be representative of, or ideally identical to, those which form the system of study, such that the data acquired are not misleading but rather correctly describe the dynamics of the main population. Because, as we discuss later in this section, it is possible to activate an extremely diverse range of materials, it is normally possible to choose identical tracers. In cases where doing so is not possible, efforts should be made to match the tracer's density, size, and material properties as closely as possible to those of the particles it is intended to represent. When tracking the motion of liquids (as opposed to granular media, which are the focus of this review), neutrally buoyant tracers are typically employed (30a).

Third, the tracer must be active enough to track reliably. Although, as discussed in Section 2.1, the precise level of activity, and hence event rate, required to track a particle accurately is dependent on the characteristic speed of the particle, for typical applications an activity level of between approximately 10 MBq and 40 MBq (300 μCi to 1,000 μCi) is used (31).[6] For activities $\lesssim$1 Bq (30 μCi) a particle can still be tracked, although finer details of its motion will typically be lost.

Finally, a tracer should—as far as possible—be free of secondary sources of $\gamma$ radiation. The presence of additional photons that are not part of a collinear pair will inherently increase the likelihood of false coincidences (see Section 2.1), creating additional noise and hence potentially lowering the accuracy of location and/or acquisition rate. In extreme cases, additional unwanted

[6]Note that for systems comprising strongly gamma-ray-attenuating materials, higher activities than those quoted will have to be used to achieve the same measured event rates and thus tracking accuracy.

radiation may begin to "blind" the detectors, i.e., providing a higher rate of incident photons than can be recorded. When producing tracers for PEPT experiments, one must bear all of these factors in mind.

There exist two main, general methods for the production of PEPT tracers: direct activation, in which activity is induced directly in the tracer material itself, and indirect activation, in which activity is induced in another medium and then applied to the tracer particle. In Section 4.3, we describe both of these methodologies in further detail.

## 4.2. Radioisotopes

There exist in nature a large number of positron-emitting radioisotopes. An ideal isotope for use in PEPT should (*a*) be short-lived enough to ensure safe disposal and avoid persistent activity in the system of study, (*b*) be long-lived enough to conduct experiments on a timescale of the order of hours without significant loss of activity, and (*c*) emit predominantly 511-keV annihilation photons to facilitate optimal precision.

Commonly used radioisotopes include fluorine-18 ($^{18}$F), sodium-22 ($^{22}$Na), cobalt-55 ($^{55}$Co), copper-61 ($^{61}$Cu), copper-64 ($^{64}$Cu), and gallium-66 ($^{66}$Ga). Of these, the most common is $^{18}$F, as this particular radioisotope does not emit any $\gamma$ radiation other than that due to $\beta^+$ annihilation. Fluorine-18 carries the additional advantage that it can be produced in any material containing oxygen via the reactions

$$^{16}\mathrm{O}\,(^{3}\mathrm{He}, p)^{18}\mathrm{F} \qquad 1.$$

and

$$^{16}\mathrm{O}\,(^{3}\mathrm{He}, n)^{18}\mathrm{Ne} \rightarrow {}^{18}\mathrm{F}. \qquad 2.$$

As such, many commonly studied granular materials such as alumina ($Al_2O_3$), glass, or sand ($SiO_2$) can be easily labeled via direct activation (see Section 4.3.1), while a host of other materials can be indirectly activated (see Section 4.3.2) using water ($H_2O$) already labeled with $^{18}$F.

In both cases, the material in which activity is to be induced is bombarded with a 33-MeV $^3$He beam from the Birmingham cyclotron in order to induce the reactions detailed above. Proton beams from the cyclotron may also be used to produce other $\beta^+$-emitting radioisotopes, for example, producing $^{55}$Co in tracers containing iron via the reaction (32)

$$^{56}\mathrm{Fe}\,(p, 2n)^{55}\mathrm{Co}. \qquad 3.$$

Of course, there exist many other possible reactions that, for brevity, are not listed here. The interested reader may find further information in References 31, 33, and 34.

## 4.3. Methods of Activation

As noted in the preceding section, particles may be labeled either directly (the particle of interest itself is irradiated with an ion beam) or indirectly (a second material is irradiated, and the activity from this material transferred onto the particle of interest). In the subsections below, we discuss both of these possibilities in greater detail.

**4.3.1. Direct activation.** In order to create a tracer via direct activation, the particle to be labeled is placed directly in the path of the ion beam used, meaning that the positron-emitting isotope is a structural element of the material used and is chemically bound to other structural elements—for example, the silicon in sand or glass (31, 33). Interactions between the ion beam

and other structural elements of the particle may give rise to additional (unwanted) short-lived isotopes, though the majority of these will decay within a time interval of ∼20 min (31, 33). As the relevant radioisotopes form a part of the structure of the tracer, and indeed the majority of these lie well within the interior of the particle, directly activated particles are highly unlikely to contaminate other objects with which they come into contact, even in the case of moderate surface degradation.

Two main limitations affect the application of direct activation. First, due to the high temperatures reached during exposure to the ion beam, particles with low melting and/or combustion temperatures (e.g., plastics or organic materials) are unsuitable for labeling using this method. Second, as the activity achieved via this method is proportional to the square of the particle diameter (31, 33), only particles with a size of $\gtrsim$1 mm can be usefully labeled in this manner.

**4.3.2. Indirect activation.** In order to create a tracer via indirect activation, the initial carrier of the $\beta^+$ must first be bombarded with the relevant ions ($^3$He in the case of water). This produces $^{18}$F in an ionic state, which can be adsorbed into materials via ion exchange or surface adsorption.

The amount of activity deposited on a particle depends on the size of the particle; the contact time; the concentration of $^{18}$F in the water; and, in the case of ion exchange, the ion-exchange capacity of the tracer material. The purity of the water is also highly important, as fluorine ions can easily be replaced by other anions that may be present in impure water. Full details of the ion-exchange process can be found in Reference 31.

## 5. THE PEPT TECHNIQUE: DERIVED PROPERTIES

In Section 2, we discuss the manner in which PEPT may be used to track the motion of a tracer through three-dimensional space. However, knowledge of the motion of a single particle is only of limited scientific value. The true power of PEPT lies in its application to ergodic, steady-state systems. For our purposes, the term ergodic can be taken to mean that the time average of the behavior of a single tracer particle moving through a system of identical particles can—if the average is taken over a period long enough to allow our particle to explore the entire system—be assumed to be representative of the ensemble-averaged behavior of all particles within the system. As a simple example, consider a system of identical, randomly moving particles split into a number of distinct regions. If a single particle spends, on average, 10% of its time in a given region, then at any given point in time one may expect 10% of all the system's particles to be located in this region. As such, for systems that obey the principle of ergodicity, the time-averaged motion of a single PEPT tracer may be used to map the whole-field, three-dimensional dynamics of an entire granular system (35),[7] extracting important physical quantities such as density, velocity and granular temperature distributions, velocity autocorrelation functions (VACFs), and diffusion coefficients. In this section, we describe the ways in which PEPT data may be manipulated in order to extract these, and various other, system properties. Note that, for simplicity, we discuss only the case of a single tracer particle, though in all instances the methods described may be easily extended to the case of multiple particles.

### 5.1. Occupancy and Density

Using PEPT data, it is possible to determine one-dimensional particle (packing) density profiles, as well as two- and three-dimensional density fields. In the subsections below, we describe how this may be achieved, as well as the possible applications of the resulting data.

[7]Note that similar results may also be achieved for transient processes by averaging large numbers of repeat experiments.

**5.1.1. Determining occupancy and density from PEPT data.** To extract occupancy or density fields from PEPT data, it is first necessary to subdivide the experimental volume into a series of individual volume elements. These can be one-dimensional slices, producing one-dimensional profiles, or two- or three-dimensional cells (or voxels), producing two- or three-dimensional fields. For simplicity, let us consider here the one-dimensional case, though the same methodology may be trivially extended to higher dimensionalities. In order to extract a one-dimensional density profile from PEPT data, the experimental volume must first be subdivided into a series of equally sized slices.

In order to create a density profile, we must then calculate the occupancy, or residence fraction, $O$, for each individual slice. The simplest manner in which the occupancy may be estimated is to sum the number of particle locations falling within each slice, and divide by the total number of particle locations recorded in the system. This is, however, a rather crude approximation, as it relies on the often dubious assumption that particle locations are evenly spaced in time. A more accurate definition of the occupancy for a given cell is the fraction of the total experimental time spent within this cell.

Under the assumption of ergodicity, the fraction of time spent by a single tracer in a given region of the system can be expected to be directly proportional to the expected fraction of the total particles in the system to be found in said region at any given time. As such, the known occupancy of the $i$th cell can be used to calculate the corresponding mean number density as

$$n_i = \frac{NO_i}{V_c}, \qquad 4.$$

where $N$ represents the total number of particles in the system and $V_c$ is the volume of a cell. Then, the packing density, $\eta_i$, can be determined as

$$\eta_i = n_i V_p, \qquad 5.$$

where $V_p$ is the volume of a particle.

By calculating $\eta_i$ for all $N_c$ cells within the system, a one-dimensional density profile can be created. Two- and three-dimensional density distributions can be created by following the same procedure but instead dividing the experimental volume into, respectively, two-dimensional pixels or three-dimensional voxels.

**5.1.2. Applications.** Knowledge of the particle density distribution within a system can be vital for determining the state of said system, either generally, as a solid, liquid, or gas (36), or more specifically, as in identifying the Leidenfrost state in vibrated systems (37) or the centrifuging state in horizontally rotated beds (38). In combination with measurements of systems' temperature and/or velocity distributions, the ability of PEPT to map one-, two-, and three-dimensional density distributions has also proven highly valuable for validating both continuum and numerical models of a variety of systems—including vibrated beds (39–41), fluidized beds (42–44), rotating-drum systems (45–48), and diverse mixer systems (49–51)—and thus extracting a wealth of additional information not directly accessible from PEPT alone. In binary or polydisperse systems, measurements of density distribution also enable the detailed study of mixing and/or segregation, as discussed further in Section 5.6. Occupancy measurements also allow analysis of residence time distributions, making them highly valuable for the study of continuous processes (52).

## 5.2. Velocity

Due to the high temporal resolution of PEPT, it is, under suitable circumstances, possible to extract pseudoinstantaneous velocity data from particle locations. In the subsections below, we discuss how these velocities may be extracted rigorously (Section 5.2.1) and subsequently how

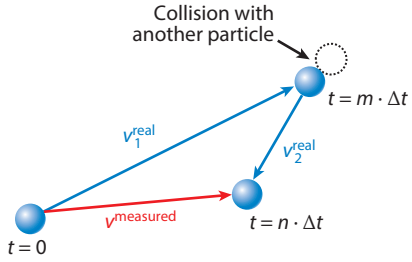


**Figure 8**

Three stages in the motion of a hypothetical tracer particle colliding with another particle at time $t = m \cdot \Delta t$. If the particle's velocity is calculated over a number of points corresponding to a total time difference $t < m \cdot \Delta t$ (where $\Delta t$ represents the average time step between locations), positron emission particle tracking (PEPT) can be expected to represent accurately the tracer's pseudoinstantaneous velocity. Conversely, for $t > m \cdot \Delta t$, the collision—which alters the particle's trajectory—will be missed, causing a false velocity to be recorded. In other words, $v_1^{real}0$ and $v_2^{real}$ are averaged out into a single velocity. A similar problem arises if the particle is convected by nonlinear fluid flow.

the velocity data acquired may be used to create velocity probability density functions (PDFs) (Section 5.2.2), spatial velocity distributions (Section 5.2.3), and velocity autocorrelation functions (Section 5.2.4). In Section 5.2.5 we discuss different methods for averaging velocities, and finally in Section 5.2.6 we discuss the various applications in which knowledge of particle velocities may be of value.

**5.2.1. Determining particle velocities from PEPT data.** As noted at the beginning of the section, PEPT data—if the temporal resolution with which they are acquired is suitably high—can be used to determine the pseudoinstantaneous velocities of particles. However, one must be careful when analyzing and interpreting PEPT velocity data for a number of reasons.

For instance, it is typically inadvisable to calculate particle velocities from a two-point average of directly adjacent particle locations. This is because a particle will typically move only a small distance, $\Delta\mathbf{r}$, in the short time step, $\Delta t$, between locations, meaning that the uncertainty on particle location becomes comparable to the distance moved, and hence the calculated velocity ($\mathbf{v} = \Delta\mathbf{r}/\Delta t$) carries a large percentage error. Conversely, if one attempts to calculate a pseudoinstantaneous velocity over too many data points (i.e., too long a time interval), one will also obtain inaccurate data if the particle experiences collisions with other particles or objects (**Figure 8**).

As such, if one wishes to use PEPT to determine accurately the instantaneous velocities of particles [or otherwise characterize a particle's ballistic motion (35)], one must ensure that the acquired data rate significantly exceeds the collision rate for the system in question. Conversely, if one is simply interested in the mean flow velocity of the system—as is most often the case—this constraint does not apply.

Particle velocities are typically determined in one of three ways, though other methods may also be applied. The simplest method is to use a center-difference approach (35):

$$\mathbf{v}_i = \frac{\mathbf{r}_{i+a} - \mathbf{r}_{i-a}}{t_{i+a} - t_{i-a}}, \qquad 6.$$

where $\mathbf{v}_i$ is the vector velocity corresponding to the $i$th location event and $a$ is an integer constant. One may also calculate velocities from PEPT data using a weighted-average approach:

$$\mathbf{v}_i = \sum_j W_j \frac{\mathbf{r}_{i+a_j} - \mathbf{r}_{i-a_j}}{t_{i+a_j} - t_{i-a_j}}, \qquad 7.$$

where $\sum W_j = 1$.

In both of the above cases, the value(s) of $a$ should be chosen to optimize the accuracy of the calculated velocities based on the activity of the tracer and the expected mean speed of particles in the system. For a highly active, slow-moving tracer, a large $a$ (i.e., averaging over many location events) may be used to give good statistics and hence low errors on the net velocity. For a fast-moving tracer and/or a low activity rate, a smaller $a$ will be required to ensure that the velocities calculated remain representative of the particle's true motion.

The final commonly employed method for calculating velocities from PEPT data is to employ a least-squares regression analysis over a suitably chosen number of points (53). Once the velocities for all location events have been determined, these microscale data may be used to provide information regarding various macroscopic properties of the system, as detailed in the following sections.

**5.2.2. Determining velocity probability density functions from PEPT data.** Granular materials, unlike classical media such as true gases, are known to exhibit non-Gaussian velocity distributions (54, 55) and anisotropic velocity/energy distributions (56)—matters of considerable scientific interest. As such, it is highly valuable to be able to obtain velocity distributions for each of a system's spatial coordinates.

Under the assumption of an ergodic system, the velocities corresponding to each location event achieved over a period $t$ can be considered equivalent to the velocities of all $N$ particles in the system over a period $t/(N\Delta t)$, where $\Delta t$ represents, as above, the mean time step between two consecutive data points. As such, velocity PDFs for the system can be created simply by appropriately sorting and normalizing the individual velocity values for all detected locations. This can be done for the $x$, $y$, and/or $z$ velocity individually or for the velocity magnitude $v = \sqrt{v_x^2 + v_y^2 + v_z^2}$.

**5.2.3. Determining spatial velocity distributions from PEPT data.** In order to determine the spatial distributions of velocities within a granular system, one must begin by subdividing the experimental volume into a series of one-, two-, or three-dimensional cells, as described in Section 5.1.

For each cell, the mean speed, as well as the mean value of each individual velocity component, can be determined by averaging the individual velocity values belonging to all location events falling within that cell. The values obtained may then be plotted to provide the desired velocity distributions. For the case of two- or three-dimensional cells, one may additionally create a velocity vector field (**Figure 9**).

**5.2.4. Determining velocity autocorrelation functions from PEPT data.** The VACF—a measure of the rate at which the velocity of a particle in a system becomes decorrelated from its initial value—is typically written as (58)

$$Z_i(t) = \langle v_i(t+s)v_i(t)\rangle; \qquad i = x, y, z, \tag{8.}$$

where $s$ represents an arbitrary period of time and the angled brackets represent an ensemble average. Of course, for PEPT, one can obtain data for only a subset of particles within a system, meaning that an ensemble average is not directly attainable. As such, one must again exploit the principle of ergodicity, enabling the use of a single, long-time trace to obtain data statistically equivalent to an ensemble average.

In order to calculate a VACF using PEPT, instead of considering a number of individual, simultaneous particle trajectories, one instead considers a series of individual slices of a single trajectory. In order to maximize statistics, these slices are typically acquired using a time-lag analysis, that is,

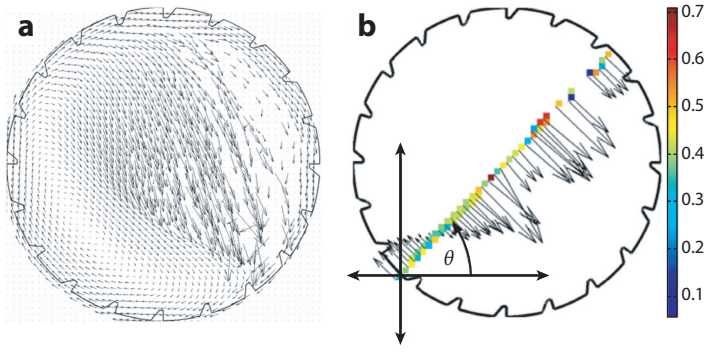


**Figure 9**

(*a*) An example (57) of a velocity vector field extracted from a rotating-drum system. The orientation of the arrows corresponds to the direction of the mean velocity vector at a given point in space, while the length of the arrows represents the velocity magnitude. (*b*) Tangential velocity profile for the system in panel *a*, along a diametrical line passing through its mean center of circulation.

a moving window translated across the particle velocity trace, creating overlapping data sets. The individual velocity correlation for the *j*th time window can be written as

$$Z_i^j = v_{i_1}^j(t + s^j)v_{i_2}^j(t). \qquad 9.$$

Here, the indices $i_1$ and $i_2$ correspond to the Cartesian coordinates $x, y$, and $z$. If $i_1 = i_2$, the quantity calculated is the autocorrelation, while if $i_1 \neq i_2$, Equation 9 gives the cross-correlation.

As PEPT inherently provides data at random time intervals, the data points for all individual traces are binned with a chosen time interval. One may arrive at the final VACF simply by averaging all of the individual traces obtained. Interestingly, the bin width can be chosen to be smaller than the mean data rate of the data being analyzed, meaning that VACFs may in fact be produced with a higher temporal resolution than the raw PEPT data used to create them. Further details regarding the extraction of VACFs from granular media using PEPT may be found in Reference 53.

**5.2.5. Face-averaged and volume-averaged particle velocities.** If it is desired to determine a spatial distribution of time-averaged particle velocity from a PEPT experiment, there are two principal ways of doing so: face averaging and volume averaging (**Figure 10**). The difference is that in face averaging only the velocities of particles whose trajectories cross a particular surface—in this case a horizontal one—are considered, whereas in volume averaging the velocities are considered for all particles located inside a specified volume within the examined time period. Xu et al. (59) consider these options in detail for both PEPT and numerically derived data for a fluidized bed, showing how different the two averages can be. The two would yield the same result if the flow were homogeneous. However, in most cases they differ due to the inherently heterogeneous structures in gas–solid flows, resulting in correlation of the local particle concentration and particle velocity.

**5.2.6. Applications.** The ability of PEPT to extract information regarding particle velocities is, unsurprisingly, valuable for a range of scientific and industrial applications. For example, analysis of the non-Gaussian nature of velocity PDFs and the decay of the VACFs in vertically vibrated systems allows insight into the fundamentals of granular dynamics (53, 60–63). In fluidized-bed

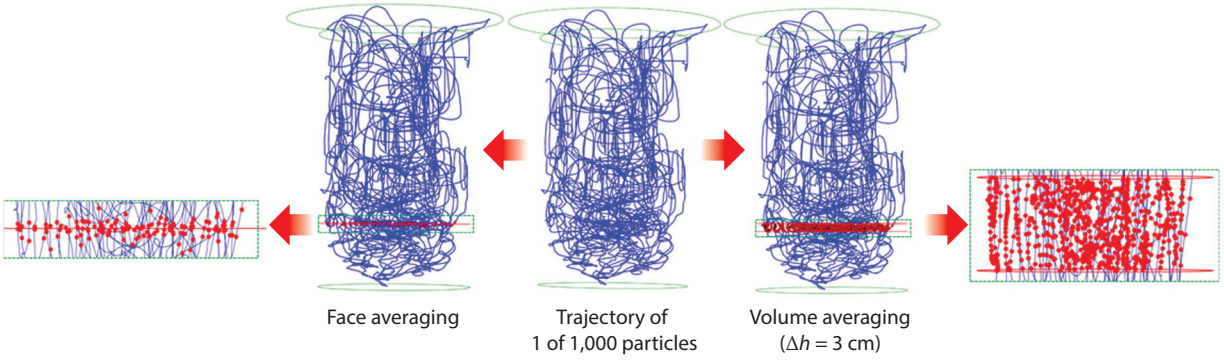


**Figure 10**

Face averaging and volume averaging of the vertical velocity component of 1 of 1,000 simulated tracer particles for a fluidized bed (59).

systems, measurements of particles' trajectories and velocities not only provide direct knowledge of a solid's motion within said systems (64–71) but also allow insight into fluid motion through, for example, analysis of particles' jump velocities and idle times (65, 72).

Velocity vector fields allow detailed insight into, for example, convective flow within vibrofluidized media (36, 61, 73–75), flow patterns and recirculation within gas-fluidized beds (64, 65, 76–78), and phase transitions in rotating-drum systems (48, 79–84). The determination of particle velocities is also crucial for the computation of other important quantities, such as shear rate (see Section 5.3) and granular temperature (see Section 5.5).

## 5.3. Shear Rate

In order to determine the shear rate, one must begin by creating a grid of velocities, as per Section 5.2.3. For simplicity, let us consider a two-dimensional velocity field corresponding to a system, such as a rotating drum (**Figure 9*a***), for which particle densities and velocities may be assumed to be constant along the third dimension—that is, the depth-averaged two-dimensional field analyzed is representative of the full three-dimensional system.

In order to analyze the shear rate, we first must choose a suitable line or plane along which we wish to calculate it. For the present example, we consider a single line of cells in a direction perpendicular to the direction of flow and bisecting the system's center of circulation (**Figure 9*b***) (85, 86), and extract the tangential velocity pertaining to each of these cells, providing a (discrete) one-dimensional velocity profile. In order to extract a shear rate from these data, we must then attempt to fit a (continuous) function to the data that accurately describes its variation. For our current example, one may utilize a function of the form

$$v_t = a_1 \sin(b_1 r + c_1) + a_2 \sin(b_2 r + c_2), \qquad 10.$$

where $r$ represents the position along the line of interest (**Figure 9*b***), and the coefficients $a_i$, $b_i$, and $c_i$ are fitting parameters. Once the values of $a_i$, $b_i$, and $c_i$ have been chosen such that Equation 10 provides a strong fit to the data, the shear rate, $\dot{\gamma}$, can be found simply by differentiating $v_t$ with respect to $r$:

$$\dot{\gamma} = a_1 b_1 \cos(b_1 r + c_1) + a_2 b_2 \cos(b_2 r + c_2). \qquad 11.$$

While the form of Equation 10, and hence of Equation 11, is specific to the system used in this example, the general principle outlined above can be applied to any system from which a shear rate is meaningfully calculable.

## 5.4. Mean Squared Displacement and Self-Diffusion

The diffusive behaviors of granular materials, and their role in processes such as mixing and segregation, are active areas of research in the field of particle technology. In this section, we discuss how particles' mean squared displacements (MSDs), self-diffusion coefficients (Section 5.4.1), and mixing behaviors (Section 5.4.2) may be extracted from PEPT data, and how this information may be utilized in real-world applications (Section 5.4.3).

**5.4.1. Determining mean squared displacement and self-diffusion from PEPT data.** As in the calculation of VACFs, described in the preceding section, the usual ensemble averages used to compute MSDs are, for PEPT analysis, replaced by averages of multiple temporal slices of a single trajectory. The classical definition of the MSD is given by

$$\text{MSD} = \langle |\mathbf{r}(t) - \mathbf{r}(0)|^2 \rangle. \quad 12.$$

In order to calculate MSD from a PEPT data set, each individual location event, $i$, may be taken as the start point, $t_i$, for an individual trace; the motion of the particle from this start point is followed for a predetermined period of time. The squared displacement for the $i$th individual trace at a time $t$ may thus be written as

$$\Delta r_i(t')^2 = |\mathbf{r}(t) - \mathbf{r}(t_i)|^2. \quad 13.$$

Each value of the squared displacement is then binned according to its relative time of location, $t' = t - t_0$, and the effective ensemble average is calculated by averaging the traces corresponding to each start point.

Using this approach, one may calculate the diffusion coefficient for a system [or indeed a region of a system (87)] in the usual manner:

$$D = \lim_{t \to \infty} \frac{1}{4t} \langle |\mathbf{r}(t) - \mathbf{r}(0)|^2 \rangle = \frac{1}{4t'N} \sum_{i=0}^{i=N} \Delta r_i(t')^2. \quad 14.$$

Further details regarding the measurement of MSD and diffusion using PEPT may be found in References 35 and 87–89.

**5.4.2. Dispersion and mixing.** PEPT is extremely well suited to the study of mixing. Many different approaches have been used, but a generic approach first proposed by Martin et al. (90) is a good starting point. This addresses the common problem of following the dispersion of a group of particles originating at the same point (**Figure 11*a***), which might represent, for example, the addition of an ingredient to a batch of product.

The difference between the trajectories is a measure of dispersion related to processes occurring at that point. In single-particle tracer studies, each time the tracer passes through a given volume element of the system, its subsequent location (some time or distance later) can be found. When the tracer has passed through each element many times, many traces are obtained with their origins at approximately the same point. Provided that the motion of the solids is time independent and the system can be considered ergodic, this is equivalent to tracing the path of many

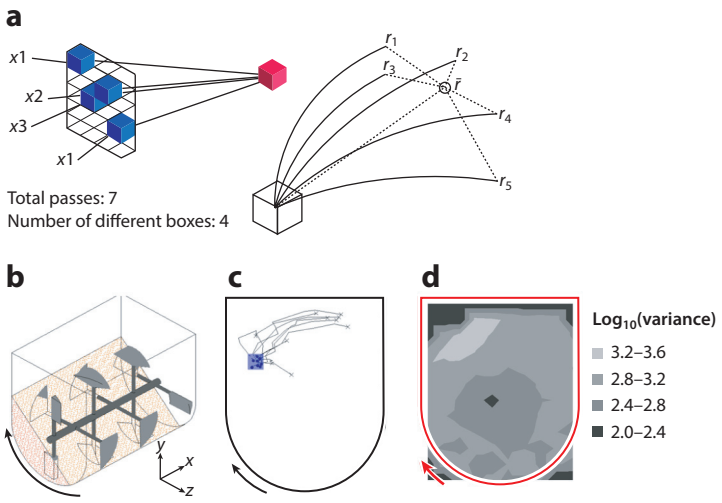


**Figure 11**

(*a*) Measuring the dispersion of a series of particles originating from the same point, or, in the case of positron emission particle tracking (PEPT), the same voxel. (*b*) A bladed mixer imaged using PEPT. (*c*) A series of individual PEPT tracks within the mixer originating from the same voxel. (*d*) Spatial distribution of the variance, calculated as per Equation 15. Lighter areas correspond to high variance and therefore high local mixing, while darker areas show little local mixing. Figure adapted from Reference 90.

particles from the same location simultaneously. **Figure 11** shows an example for a mixer with a high-speed rotating blade.

The variance between the locations is then given by

$$\sigma^2 = \frac{1}{n}\sum_{i=1}^{n}(x_i - \bar{x})^2 + (y_i - \bar{y})^2 + (z_i - \bar{z})^2, \qquad 15.$$

where $\sigma$ denotes standard deviation; $\bar{x}, \bar{y}$, and $\bar{z}$ denote mean final location; and $n$ is the number of trajectories. The logarithm of the local variance is plotted in **Figure 11*d*** for the particular mixer in question.

A question arises as to how far (or for how long) the tracer particle should be allowed to move before its location variance is found. First, time is a more appropriate measure for the interval between the start point and the variance measurement, and is consistent with the approach taken in diffusion. Second, the elapsed time should be long enough to allow measurable movement to take place, but not so long that that movement is no longer related to the conditions that are local to the point of interest.

**5.4.3. Applications.** Measures of self-diffusion or dispersion are widely used as a proxy measurement to establish the quality or rate of mixing within a system. PEPT has been used to this end in a variety of tumbling mixers, v-mixers (91, 92), rotating-drum mixers (46, 93), high-shear mixer-granulators (94, 95), bladed mixers (96, 97), and paddle mixers (90, 98, 99). MSD measurements can also be used to indicate the state of a system by showing signatures of ballistic motion (indicating a dilute, energetic system) (100, 101) or caging (102), indicating a dense granular liquid close to the jamming transition (36).

## 5.5. Granular Temperature

When discussing the concept of granular temperature, it is important to note that there exist several possible definitions thereof (103, 104). In this review, we adopt the definition used by Ogawa (105, 106), which is both the most commonly employed and the most literal analog to the classical temperature: the mean fluctuation energy of particles within a system, given mathematically as (103)

$$T = \frac{1}{D} m \langle c^2 \rangle, \qquad 16.$$

where $m$ is the mass of an individual particle, $D$ is an integer representing the dimensionality of the system ($D = 1, 2$, or 3 for a one-, two-, or three-dimensional system, respectively), and $c$ is the fluctuation velocity of a particle about the mean:

$$c = v - \bar{v}. \qquad 17.$$

**5.5.1. Dilute systems.** For dilute systems, where the acquisition rate, $\tau_a$, of PEPT data greatly exceeds the particle collision rate, $\tau_c$, the granular temperature of a system (or region thereof) can be simply calculated using the formulation given in Equation 16. Below we show how, for this case, a spatial granular temperature distribution may be obtained from PEPT data.

First, the mean velocity for a given region (cell) can be calculated as described in Section 5.2.3. Second, this mean velocity can be compared with the pseudoinstantaneous velocities corresponding to each data point lying inside the cell to calculate a series of fluctuation velocities, the average of which can be used to determine the mean granular temperature as per Equation 16. By repeating this process for all cells, the spatial variation of $T$ across the system may be mapped.

**5.5.2. Denser systems.** For cases in which the assumption $\tau_a \gg \tau_c$ does not hold, the inability of PEPT to detect collision events reliably will introduce significant errors into the calculation of velocities, and hence $T$, as detailed in Section 5.2.1. In this case, an alternative approach may be adopted (87, 89), in which the mean squared speed required to calculate $T$ can be acquired using the MSD:

$$\langle c^2 \rangle t^2 = \langle |\mathbf{r}(t) - \mathbf{r}(0)|^2 \rangle. \qquad 18.$$

The MSD, $\langle |\mathbf{r}(t) - \mathbf{r}(0)|^2 \rangle$, can be calculated from PEPT data as described in Section 5.4. Note that whereas the diffusion coefficient is calculated from the long-time, diffusive part of the MSD, the mean squared speed is extracted from the short-time, ballistic region (89).

**5.5.3. Applications.** PEPT measurements of granular temperature are more common in academic, as opposed to industrial, research, where they are widely used to draw parallels with the behaviors of classical molecular systems (60, 61, 107–109) and thus help develop, test, and validate theoretical frameworks (39, 110, 111). PEPT was the first technique to measure the temperature of a three-dimensional granular fluid (35), the first to provide insight into temperature scaling in three-dimensional systems (87), and the first to demonstrate directly that binary granular beds violate the equipartition theorem (112).

## 5.6. Properties of Binary and Polydisperse Systems

In the preceding subsections, we have implicitly considered only monodisperse systems. PEPT can also, however, be easily applied to binary and ternary systems, and indeed those possessing

higher orders of polydispersity (120). In this section, we discuss the two main methods by which this may be achieved, the comparative strengths and weaknesses of each method, and the manner in which these methods may be used to measure and quantify certain key quantities pertaining exclusively to binary or polydisperse systems.

**5.6.1. Acquiring data from multiple species.** PEPT data may be acquired from particles possessing two or more individual species in two distinct ways: by repeating the same experiment multiple times with different tracers or simply by running a single experiment using multiple labeled particles (see also Section 2.2). We provide an overview of each methodology in the subsections below.

***5.6.1.1. Single-tracer method.*** The most widely used method to study polydisperse systems using PEPT is, for a system containing $N_s$ distinct species of particle, to repeat the relevant experiment under identical conditions $N_s$ times, with each repeat utilizing a tracer of a different species. Under the assumption of ergodicity and suitably long imaging times in all cases, the combined time averages of these $N_s$ separate runs can be considered equivalent to those of a single run tracking all $N_s$ particles.

Consider, as an example, the case of a binary mixture of equally sized particles differing in their material properties. If one were to conduct two identical experiments of equal duration (one for each tracer species), the packing density of each individual species could be found in a manner identical to that described in Section 5.1, except that the $N$ used in Equation 4, representing the total number of particles in the system, must now be replaced with $N_i$, the number of the current ($i$th) species of interest. If we consider instead the case in which particles also differ in size, it is important to ensure the use of the correct particle volume, $V_p$, for each case studied when applying Equation 5. The methods for calculating the other quantities listed in this section can be adapted to the binary or polydisperse case with equal simplicity.

The main advantage of the single-tracer method is that, as each species is measured in isolation, both the spatial and temporal resolution of the data acquired remain maximal. However, the method is—compared with the multiple-tracer case—considerably more time-consuming, scaling linearly with the number of species used. As such, this method is infeasible for the imaging of highly polydisperse systems.

***5.6.1.2. Multiple-tracer method.*** The multiple-tracer method, though conceptually simpler than the single-tracer method, is currently less widely used. However, as multiple-particle tracking techniques evolve and develop (see Section 2.2), this may change in the coming years.

In this method, one or more tracers of each species are introduced to the same system and imaged simultaneously. The main complication with this technique arises from the fact that—unlike with multiple-particle tracking in the monodisperse case (see Section 2.2)—the ability to distinguish between different tracers is no longer optional but vital. As such, one must be sure to utilize tracers of clearly differing activity, a task that becomes even more complex if one is utilizing particles labeled with isotopes of differing half-lives. Assuming that different species may be successfully separated, relevant quantities may be extracted from these data in the same manner as described in the preceding section.

As alluded to above, the multiple-tracer method is faster—in some cases significantly so—than the single-tracer method, and carries the additional advantage of being able to provide a degree of insight into the interactions between differing species. Its main disadvantage—other than the abovementioned necessity of utilizing distinct activities—is that the temporal and/or

spatial accuracy of tracking will typically [but not always (20)] decrease with the increasing number of particles used, an issue discussed in detail in Section 2.2.

**5.6.2. Single-species concentration distributions and segregation.** When studying binary and polydisperse systems, one of the most significant and widely explored (113) phenomena is that of granular segregation, the process by which particles of differing species spontaneously migrate to different regions of a system (114). If one wishes to assess the extent of segregation in a system, it is first valuable to determine the spatial distributions of different particle species and their relative concentration throughout the system. In order to do so, one must subdivide the experimental volume into cells and determine the individual spatial packing-density distributions for each species within the system, as described in Section 5.1. For the *k*th cell within the system, the local fractional concentration of particles of species *i* can be determined as

$$\phi_i^k = \frac{\eta_i^k}{\sum_j^{N_s} \eta_j^k}, \tag{19.}$$

where $N_s$ represents the total number of distinct particle species in the system. For the most common case of a binary system containing two species, *a* and *b*, the above equation reduces to

$$\phi_a^k = \frac{\eta_a^k}{\eta_a^k + \eta_b^k}, \qquad \phi_b^k = \frac{\eta_b^k}{\eta_a^k + \eta_b^k}. \tag{20.}$$

Note that these equations provide a measure of the single-species concentration in terms of the relative volume fraction of a given species. One can compute the corresponding number fraction by using the same equations, simply replacing the packing fraction $\eta$ with the number density $n$. By determining the concentration of a given species for all cells within a system, one may build up a concentration distribution such as that shown in **Figure 12**.

With a known concentration distribution, one may then attempt to quantify the degree of segregation exhibited by a system using a quantity such as the segregation intensity parameter, $I_s$. For a system subdivided into $N_c$ equally sized cells, $I_s$ may be calculated as

$$I_s = \left[ \frac{1}{N_c} \sum_{k=1}^{k=N_c} \left( \phi_i^k - \phi_i^m \right)^2 \right]^{\frac{1}{2}}, \tag{21.}$$

where $\phi_i^k$ is the concentration (either volume or number) of species *i* in cell *k*, and $\phi_i^m$ is the mean concentration of this species in the system as a whole. For a 50:50 binary mixture of particles, a completely segregated system will yield a value $I_s = 0.5$, and a perfectly mixed system will yield $I_s = 0$. For different relative concentrations of particle species, while the value of $I_s$ corresponding to perfect mixing will remain consistent, the value pertaining to perfect segregation may vary (though it will always correspond to the maximum value achievable). As such, if one wishes to compare the segregative behaviors of systems with differing overall concentrations of individual species, the $I_s$ values for each different system must be normalized.

Note also that the precise value of $I_s$ achieved from a given system is cell size dependent—or, more specifically, dependent on the size of the cells relative to the particles used. In other words, while the values of $I_s$ can be expected to remain self-consistent for a fixed grid and system composition, one must take care when attempting direct, quantitative comparison between results in the literature using differing cell sizes and/or particle sizes.

Although the segregation intensity, $I_s$, was the most commonly used parameter in previous PEPT studies of segregation, there exist several alternative scalar measures that may be applied to

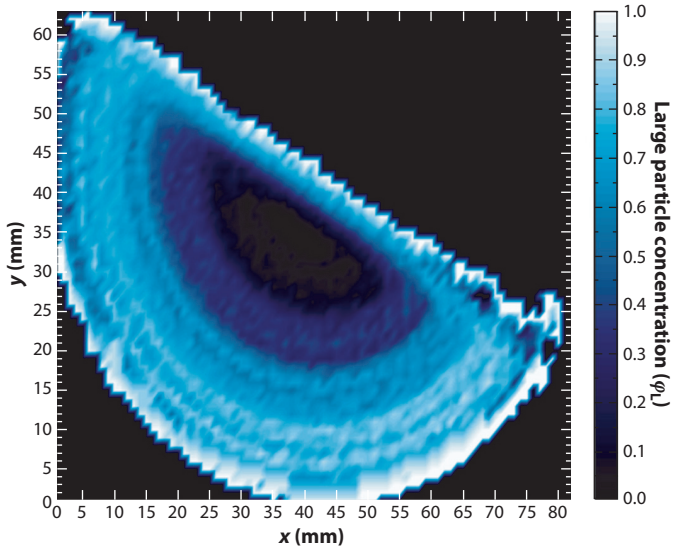


**Figure 12**

Positron emission particle tracking (PEPT) image (45) showing the well-known radial segregation pattern (115) exhibited by a binary granular bed housed in a rotating drum. In the image, lighter (darker) regions correspond to regions of higher (lower) large-particle concentration, $\phi_L$.

PEPT data. The interested reader may find details of some common alternative parameters, and how they are computed, in References 116–118.

**5.6.3. Temperature partition.** Another widely studied phenomenon unique to binary and polydisperse granular systems, and indeed another major characteristic separating them from classical systems, is the nonequipartition of energy between different species coexisting in a single system (112, 119). The extent of nonequipartition may in fact be relatively easily characterized by determining the granular temperatures individually for both/all components of a given system, as per Section 5.5, and by finding the ratio(s) between these values. This can be performed either on a whole-field basis or by comparing temperatures cell by cell in order to explore the potential variation of equipartition through different regions of a system.

**5.6.4. Applications.** The ability to track the distribution of one or more components of a mixture through a system may be valuable for any process in which the homogenization or separation of such a system is desirable. PEPT has already been used in this manner in vibrated systems (107, 120–123); rotating drums (45, 46, 93); bladed mixers (99); and, more recently, gas-fluidized beds (124, 124a), though the technique may easily be applied to many other industrially relevant systems in which mixing and segregation are significant issues.

## 5.7. System-Specific Quantities

In the preceding sections, we have described the most widely applicable and commonly utilized quantities that may be extracted from PEPT data. Nonetheless, there exist a host of other, more system-specific and/or more infrequently applied quantities—for example, convection strength in

vibrated beds (36, 61, 125–127), turnover rate in fluidized beds (128), and free-surface angle in rotating drums (80, 81)—which may also be characterized using PEPT.

## SUMMARY POINTS

1. New algorithms increasing the number of particles that may be tracked simultaneously (and decreasing the minimum separation distance above which separate trajectories may be successfully distinguished) have greatly improved the applicability of PEPT to transient processes, as well as the ability of the technique to track rotational motion.
2. With the availability of a variety of different scanner types adapted for PEPT use—ranging from small-animal scanners capable of imaging comparatively small systems with extremely high spatial resolution to modular systems capable of the in situ imaging of industrial-scale systems of arbitrary geometry—the PEPT technique is now more broadly applicable than ever before.
3. Improvements in the techniques used to label tracers with radioactivity have made it possible to track noninvasively an almost unlimited range of materials and to reconstruct with accuracy the dynamics of particles with sizes as small as 50 μm.
4. Thanks to the combined efforts of numerous researchers working in diverse fields, algorithms have been developed to extract an expansive range of physical quantities—both fundamental and highly system specific—from PEPT data, allowing past, current, and future researchers to explore a vast number of phenomena and processes in a diverse array of granular and multiphase systems.

## FUTURE ISSUES

1. Super-PEPT: A new, custom-built detector array is currently under development at the University of Birmingham. The system is expected to achieve data rates of $2 \times 10^6$ events per second with a spatial resolution of 1 mm across a field of view 400 mm in diameter and 480 mm in height.
2. Multimodal imaging: Although a powerful technique, PEPT—like all experimental imaging methods—possesses inherent limitations. Combining or even hybridizing PEPT with other techniques that have complementary capabilities could enable the acquisition of more complete information from a variety of granular systems.
3. Cross-comparison of algorithms: As outlined in Section 2.2, there exist various algorithms with which PEPT data may be preprocessed. However, as these algorithms have been developed and tested using decidedly dissimilar detector systems, a direct comparison between them cannot be reliably drawn from existing literature. Future research explicitly comparing the algorithms, and their relative effectiveness under different conditions and for different applications, would prove highly useful to the field.
4. Tracer miniaturization: At present, tracers with sizes down to 50 μm have been successfully synthesized and tracked. However, further miniaturization of PEPT tracers will make the technique more valuable for a greater range of applications, in particular biomedical applications.

## DISCLOSURE STATEMENT

The authors are not aware of any affiliations, memberships, funding, or financial holdings that might be perceived as affecting the objectivity of this review.

## ACKNOWLEDGMENTS

The authors gratefully acknowledge funding from the UK Engineering and Physical Sciences Research Council, and from a large number of industrial sponsors, which has been essential to many of the developments described here.

## LITERATURE CITED

1. Hawkesworth M, O'Dwyer M, Walker J, Fowles P, Heritage J, et al. 1986. A positron camera for industrial application. *Nucl. Instrum. Methods A* 253:145–57
2. Bemrose C, Fowles P, Hawkesworth M, O'Dwyer M. 1988. Application of positron emission tomography to particulate flow measurement in chemical engineering processes. *Nucl. Instrum. Methods A* 273:874–80
3. Hawkesworth M, Parker DJ, Fowles P, Crilly J, Jefferies N, Jonkers G. 1991. Nonmedical applications of a positron camera. *Nucl. Instrum. Methods A* 310:423–34
4. Parker DJ, Broadbent C, Fowles P, Hawkesworth M, McNeil P. 1993. Positron emission particle tracking—a technique for studying flow within engineering equipment. *Nucl. Instrum. Methods A* 326:592–607
5. Palmer MR, Brownell GL. 1992. Annihilation density distribution calculations for medically important positron emitters. *IEEE Trans. Med. Imaging* 11:373–78
6. Tsoulfanidis N. 2010. *Measurement and Detection of Radiation*. Boca Raton, FL: CRC
7. Parker DJ, Forster R, Fowles P, Takhar P. 2002. Positron emission particle tracking using the new Birmingham positron camera. *Nucl. Instrum. Methods A* 477:540–45
8. Parker DJ. 2017. Positron emission particle tracking and its application to granular media. *Rev. Sci. Instrum.* 88:051803
9. Yang Z, Parker DJ, Fryer P, Bakalis S, Fan X. 2006. Multiple-particle tracking: an improvement for positron particle tracking. *Nucl. Instrum. Methods A* 564:332–38
10. Yang Z, Fryer P, Bakalis S, Fan X, Parker DJ, Seville J. 2007. An improved algorithm for tracking multiple, freely moving particles in a positron emission particle tracking system. *Nucl. Instrum. Methods A* 577:585–94
11. Bickell M, Buffler A, Govender I, Parker DJ. 2012. A new line density tracking algorithm for PEPT and its application to multiple tracers. *Nucl. Instrum. Methods A* 682:36–41
12. Hamerly G, Elkan C. 2004. Learning the *k* in *k*-means. In *Proceedings of the 16th International Conference on Neural Information Processing Systems* (*NIPS03*), pp. 281–88. New York: ACM
13. MacQueen J. 1967. Some methods for classification and analysis of multivariate observations. In *Proceedings of the 5th Berkeley Symposium on Mathematical Statistics and Probability*, Vol. 1, pp. 281–97. Berkeley: Univ. Calif. Press
14. Anderson TW, Darling DA. 1952. Asymptotic theory of certain "goodness of fit" criteria based on stochastic processes. *Ann. Math. Stat.* 23:193–212
15. Wiggins C, Santos R, Ruggles A. 2017. A feature point identification method for positron emission particle tracking with multiple tracers. *Nucl. Instrum. Methods A* 843:22–28
16. Crocker JC, Grier DG. 1996. Methods of digital video microscopy for colloidal studies. *J. Colloid Interface Sci.* 179:298–310
17. Sbalzarini IF, Koumoutsakos P. 2005. Feature point tracking and trajectory analysis for video imaging in cell biology. *J. Struct. Biol.* 151:182–95
18. Blakemore D, Govender I, McBride A, Mainza A. 2019. Multiple particle tracking in PEPT using Voronoi tessellations. *Chem. Eng. Sci.* 207:780–89

19. Aurenhammer F. 1991. Voronoi diagrams: a survey of a fundamental geometric data structure. *ACM Comput. Surv.* 23:345–405
20. Nicuşan A, Windows-Yule C. 2020. Positron emission particle tracking using machine learning. *Rev. Sci. Instrum.* 91:013329
21. Mandel S. 2020. Machine learning is used to conduct positron emission particle tracking. *AIP Scilight*, Jan. 24
22. Campello RJ, Moulavi D, Sander J. 2013. Density-based clustering based on hierarchical density estimates. In *Proceedings of the Pacific-Asia Conference on Knowledge Discovery and Data Mining*, pp. 160–72. Berlin: Springer
23. Parker DJ, Hawkesworth M, Broadbent C, Fowles P, Fryer T, McNeil P. 1994. Industrial positron-based imaging: principles and applications. *Nucl. Instrum. Methods A* 348:583–92
24. Parker DJ, Allen D, Benton D, Fowles P, McNeil P, et al. 1997. Developments in particle tracking using the Birmingham positron camera. *Nucl. Instrum. Methods A* 392:421–426
25. Cole K, Buffler A, Van der Meulen N, Cilliers J, Franzidis J, et al. 2012. Positron emission particle tracking measurements with 50 micron tracers. *Chem. Eng. Sci.* 75:235–42
26. Spinks T, Jones T, Bloomfield P, Bailey D, Miller M, et al. 2000. Physical characteristics of the ECAT EXACT3D positron tomograph. *Phys. Med. Biol.* 45:2601–18
27. Langford S, Wiggins C, Tenpenny D, Ruggles A. 2016. Positron emission particle tracking (PEPT) for fluid flow measurements. *Nucl. Eng. Des.* 302:81–89
28. Tai YC, Chatziioannou A, Siegel S, Young J, Newport D, et al. 2001. Performance evaluation of the microPET P4: a PET system dedicated to animal imaging. *Phys. Med. Biol.* 46:1845–62
29. Sadrmomtaz A, Parker DJ, Byars L. 2007. Modification of a medical PET scanner for PEPT studies. *Nucl. Instrum. Methods A* 573:91–94
30. Parker DJ, Leadbeater T, Fan X, Hausard M, Ingram A, Yang Z. 2009. Positron emission particle tracking using a modular positron camera. *Nucl. Instrum. Methods A* 604:339–42

30a. Fairhurst PG, Barigou M, Fryer PJ, Pain JP, Parker DJ. 2001. Using positron emission particle tracking (PEPT) to study nearly neutrally buoyant particles in high solid fraction pipe flow. *Int. J. Multiph. Flow* 27(11):1881–901

31. Fan X, Parker DJ, Smith M. 2006. Labelling a single particle for positron emission particle tracking using direct activation and ion-exchange techniques. *Nucl. Instrum. Methods A* 562:345–50
32. Lagunas-Solar M, Jungerman J. 1979. Cyclotron production of carrier-free cobalt-55, a new positron-emitting label for bleomycin. *Int. J. Appl. Radiat. Isot.* 30:25–32
33. Parker DJ, Fan X. 2008. Positron emission particle tracking application and labelling techniques. *Particuology* 6:16–23
34. Miller PW, Long NJ, Vilar R, Gee AD. 2008. Synthesis of $^{11}$C, $^{18}$F, $^{15}$O, and $^{13}$N radiolabels for positron emission tomography. *Angew. Chem. Int. Ed.* 47:8998–9033
35. Wildman R, Huntley J, Hansen JP, Parker DJ, Allen D. 2000. Single-particle motion in three-dimensional vibrofluidized granular beds. *Phys. Rev. E* 62:3826
36. Windows-Yule CRK, Rosato AD, Rivas N, Parker DJ. 2014. Influence of initial conditions on granular dynamics near the jamming transition. *New J. Phys.* 16:063016
37. Windows-Yule C, Rivas N, Parker DJ, Thornton A. 2014. Low-frequency oscillations and convective phenomena in a density-inverted vibrofluidized granular system. *Phys. Rev. E* 90:062205
38. Juarez G, Chen P, Lueptow RM. 2011. Transition to centrifuging granular flow in rotating tumblers: a modified Froude number. *New J. Phys.* 13:053055
39. Martin T, Huntley J, Wildman R. 2005. Hydrodynamic model for a vibrofluidized granular bed. *J. Fluid Mech.* 535:325–45
40. Viswanathan H, Sheikh NA, Wildman RD, Huntley JM. 2011. Convection in three-dimensional vibrofluidized granular beds. *J. Fluid Mech.* 682:185–212
41. Viswanathan H, Wildman R, Huntley J, Martin T. 2006. Comparison of kinetic theory predictions with experimental results for a vibrated three-dimensional granular bed. *Phys. Fluids* 18:113302
42. Hoomans B, Kuipers J, Salleh MM, Stein M, Seville J. 2001. Experimental validation of granular dynamics simulations of gas-fluidised beds with homogenous in-flow conditions using positron emission particle tracking. *Powder Technol.* 116:166–77

43. Seiler C, Fryer P, Seville J. 2008. Statistical modelling of the spouted bed coating process using positron emission particle tracking (PEPT) data. *Can. J. Chem. Eng.* 86:571–81
44. Epstein N, Grace JR. 2010. *Spouted and Spout-Fluid Beds: Fundamentals and Applications*. Cambridge, UK: Cambridge Univ. Press
45. González S, Windows-Yule C, Luding S, Parker DJ, Thornton AR. 2015. Forced axial segregation in axially inhomogeneous rotating systems. *Phys. Rev. E* 92:022202
46. Windows-Yule C, Scheper B, van der Horn A, Hainsworth N, Saunders J, et al. 2016. Understanding and exploiting competing segregation mechanisms in horizontally rotated granular media. *New J. Phys.* 18:023013
47. Yang R, Zou R, Yu A. 2003. Microdynamic analysis of particle flow in a horizontal rotating drum. *Powder Technol.* 130:138–46
48. Govender I, Pathmathas T. 2016. A positron emission particle tracking investigation of the flow regimes in tumbling mills. *J. Phys. D* 50:035601
49. Marigo M, Davies M, Leadbeater T, Cairns D, Ingram A, Stitt E. 2013. Application of positron emission particle tracking (PEPT) to validate a discrete element method (DEM) model of granular flow and mixing in the Turbula mixer. *Int. J. Pharm.* 446:46–58
50. Alizadeh E, Bertrand F, Chaouki J. 2014. Comparison of DEM results and Lagrangian experimental data for the flow and mixing of granules in a rotating drum. *AIChE J.* 60:60–75
51. Stewart R, Bridgwater J, Zhou Y, Yu A. 2001. Simulated and measured flow of granules in a bladed mixer—a detailed comparison. *Chem. Eng. Sci.* 56:5457–71
52. Parker DJ, Fan X, Forster RN, Fowles P, Ding Y, Seville JP. 2005. Positron imaging studies of rotating drums. *Can. J. Chem. Eng.* 83:83–87
53. Wildman R, Hansen JP, Parker DJ. 2002. Velocity auto-correlation functions in three-dimensional vibro-fluidized granular beds. *Phys. Fluids* 14:232–39
54. Puglisi A, Loreto V, Marconi UMB, Petri A, Vulpiani A. 1998. Clustering and non-Gaussian behavior in granular matter. *Phys. Rev. Lett.* 81:3848
55. Olafsen J, Urbach JS. 1999. Velocity distributions and density fluctuations in a granular gas. *Phys. Rev. E* 60:R2468–71
56. van der Meer D, Reimann P. 2006. Temperature anisotropy in a driven granular gas. *Europhys. Lett.* 74:384–90
57. Govender I, Mangesana N, Mainza A, Franzidis JP. 2011. Measurement of shear rates in a laboratory tumbling mill. *Miner. Eng.* 24:225–29
58. Hansen JP, McDonald IR. 1990. *Theory of Simple Liquids*. Amsterdam: Elsevier
59. Xu Y, Li T, Lu L, Tebianian S, Chaouki J, et al. 2019. Numerical and experimental comparison of tracer particle and averaging techniques for particle velocities in a fluidized bed. *Chem. Eng. Sci.* 195:356–66
60. Windows-Yule CRK, Parker DJ. 2013. Boltzmann statistics in a three-dimensional vibrofluidized granular bed: idealizing the experimental system. *Phys. Rev. E* 87:022211
61. Windows-Yule C, Rivas N, Parker DJ. 2013. Thermal convection and temperature inhomogeneity in a vibrofluidized granular bed: the influence of sidewall dissipation. *Phys. Rev. Lett.* 111:038001
62. Windows-Yule C, Maddox B, Parker DJ. 2014. The role of rotational inertia in the dynamics of vibrofluidised granular gases. *Europhys. Lett.* 108:58006
63. Windows-Yule C. 2017. Do granular systems obey statistical mechanics? A review of recent work assessing the applicability of equilibrium theory to vibrationally excited granular media. *Int. J. Mod. Phys. B* 31:1742010
64. Stein MG. 1999. *Particle motion in fluidised beds*. PhD Diss., Univ. Birmingham, Birmingham, UK
65. Stein M, Ding Y, Seville J, Parker DJ. 2000. Solids motion in bubbling gas fluidised beds. *Chem. Eng. Sci.* 55:5291–300
66. Fan X, Parker DJ, Yang Z, Seville JP, Baeyens J. 2008. The effect of bed materials on the solid/bubble motion in a fluidised bed. *Chem. Eng. Sci.* 63:943–50
67. Fan X, Yang Z, Parker DJ. 2011. Impact of solid sizes on flow structure and particle motions in bubbling fluidization. *Powder Technol.* 206:132–38

68. Seville J, Salleh A, Ingram A, McCormack A, Greenwood R, Reiling V. 2004. Particle motion and defluidisation by sintering in the fluidised bed polyethylene process. In *Proceedings of the 11th International Conference on Fluidization* (*Fluidization XI*), pp. 211–18. Brooklyn, NY: Eng. Conf. Int.
69. Ingram I, Hausard M, Fan X, Parker DJ, Seville J, et al. 2007. Portable positron emission particle tracking (PEPT) for industrial use. In *Proceedings of the 12th International Conference on Fluidization: New Horizons in Fluidization Engineering* (*Fluidization XII*), pp. 497–504. Brooklyn, NY: Eng. Conf. Int.
70. Chan CW, Seville JP, Parker DJ, Baeyens J. 2010. Particle velocities and their residence time distribution in the riser of a CFB. *Powder Technol.* 203:187–97
71. Chan CW, Seville JP, Fan X, Baeyens J. 2008. Particle motion in CFB cyclones as observed by positron emission particle tracking. *Ind. Eng. Chem. Res.* 48:253–61
72. Seville J, Silomon-Pflug H, Knight P. 1998. Modelling of sintering in high temperature gas fluidisation. *Powder Technol.* 97:160–69
73. Wildman R, Huntley J, Parker DJ. 2001. Convection in highly fluidized three-dimensional granular beds. *Phys. Rev. Lett.* 86:3304–7
74. Wildman RD, Martin TW, Krouskop PE, Talbot J, Huntley JM, Parker DJ. 2005. Convection in vibrated annular granular beds. *Phys. Rev. E* 71:061301
75. Windows-Yule CRK, Lanchester E, Madkins D, Parker DJ. 2018. New insight into pseudo-thermal convection in vibrofluidised granular systems. *Sci. Rep.* 8:12859
76. Li Y, Fan H, Fan X. 2014. Identify of flow patterns in bubbling fluidization. *Chem. Eng. Sci.* 117:455–64
77. Li L, Rasmuson A, Ingram A, Johansson M, Remmelgas J, et al. 2015. PEPT study of particle cycle and residence time distributions in a Würster fluid bed. *AIChE J.* 61:756–68
78. Hensler T, Tupy M, Strer T, Pöschel T, Wirth KE. 2015. Particle tracking in fluidized beds with secondary gas injection. *Proc. Eng.* 102:850–57
79. Ding Y, Forster R, Seville J, Parker DJ. 2002. Granular motion in rotating drums: bed turnover time and slumping–rolling transition. *Powder Technol.* 124:18–27
80. Lim SY, Davidson J, Forster R, Parker DJ, Scott D, Seville J. 2003. Avalanching of granular material in a horizontal slowly rotating cylinder: PEPT studies. *Powder Technol.* 138:25–30
81. Morrison A, Govender I, Mainza A, Parker DJ. 2016. The shape and behaviour of a granular bed in a rotating drum using Eulerian flow fields obtained from PEPT. *Chem. Eng. Sci.* 152:186–98
82. Ancey C. 2001. Dry granular flows down an inclined channel: experimental investigations on the frictional–collisional regime. *Phys. Rev. E* 65:011304
83. Govender I, Richter MC, Mainza AN, De Klerk DN. 2017. A positron emission particle tracking investigation of the scaling law governing free surface flows in tumbling mills. *AIChE J.* 63:903–13
84. Laverman J, Fan X, Ingram A, van Sint Annaland M, Parker DJ, et al. 2012. Experimental study on the influence of bed material on the scaling of solids circulation patterns in 3D bubbling gas–solid fluidized beds of glass and polyethylene using positron emission particle tracking. *Powder Technol.* 224:297–305
85. McBride A, Govender I, Powell M, Cloete T. 2004. Contributions to the experimental validation of the discrete element method applied to tumbling mills. *Eng. Comput.* 21:119–36
86. Govender I, McBride A, Powell M. 2004. Improved experimental tracking techniques for validating discrete element method simulations of tumbling mills. *Exp. Mech.* 44:593–607
87. Wildman R, Huntley J, Parker DJ. 2001. Granular temperature profiles in three-dimensional vibrofluidized granular beds. *Phys. Rev. E* 63:061311
88. Wildman R, Huntley J, Hansen JP. 1999. Self-diffusion of grains in a two-dimensional vibrofluidized bed. *Phys. Rev. E* 60:7066–75
89. Wildman R, Huntley J. 2000. Novel method for measurement of granular temperature distributions in two-dimensional vibro-fluidised beds. *Powder Technol.* 113:14–22
90. Martin T, Seville J, Parker DJ. 2007. A general method for quantifying dispersion in multiscale systems using trajectory analysis. *Chem. Eng. Sci.* 62:3419–28
91. Kuo H, Knight P, Parker DJ, Tsuji Y, Adams M, Seville J. 2002. The influence of DEM simulation parameters on the particle behaviour in a v-mixer. *Chem. Eng. Sci.* 57:3621–38
92. Kuo H, Knight P, Parker DJ, Seville J. 2005. Solids circulation and axial dispersion of cohesionless particles in a v-mixer. *Powder Technol.* 152:133–40

93. Windows-Yule C, Van Der Horn A, Tunuguntla D, Parker DJ, Thornton A. 2017. Inducing axial banding in bidisperse-by-density granular systems using noncylindrical tumbler geometries. *Phys. Rev. Appl.* 8:024010
94. Ng B, Kwan C, Ding Y, Ghadiri M, Fan X, Parker DJ. 2008. Granular flow fields in vertical high shear mixer granulators. *AIChE J.* 54:415–26
95. Knight P, Seville J, Wellm A, Instone T. 2001. Prediction of impeller torque in high shear powder mixers. *Chem. Eng. Sci.* 56:4457–71
96. Stewart R, Bridgwater J, Parker DJ. 2001. Granular flow over a flat-bladed stirrer. *Chem. Eng. Sci.* 56:4257–71
97. Bridgwater J, Broadbent C, Parker DJ. 1993. Study of the influence of blade speed on the performance of a powder mixer using positron emission particle tracking. *Chem. Eng. Res. Des.* 71:675–81
98. Jones J, Parker DJ, Bridgwater J. 2007. Axial mixing in a ploughshare mixer. *Powder Technol.* 178:73–86
99. Laurent B, Bridgwater J, Parker DJ. 2002. Convection and segregation in a horizontal mixer. *Powder Technol.* 123:9–18
100. Wildman RD, Huntley JM, Jean-Pierre H. 2001. Experimental studies of vibro-fluidised granular beds. In *Granular Gases*, ed. T Pöschel, S Luding, pp. 215–32. Berlin: Springer
101. Marston JO, Thoroddsen ST. 2015. Investigation of granular impact using positron emission particle tracking. *Powder Technol.* 274:284–88
102. Keys AS, Abate AR, Glotzer SC, Durian DJ. 2007. Measurement of growing dynamical length scales and prediction of the jamming transition in a granular material. *Nat. Phys.* 3:260–64
103. Goldhirsch I. 2008. Introduction to granular temperature. *Powder Technol.* 182:130–36
104. Behringer B. 2002. Granular materials: taking the temperature. *Nature* 415:594–95
105. Ogawa S. 1978. Multitemperature theory of granular materials. In *Proceedings of the US–Japan Seminar on Continuum Mechanical and Statistical Approaches in the Mechanics of Granular Materials*, pp. 208–17. Tokyo: Gakujutsu Bunken Fukyukai
106. Ogawa S, Umemura A, Oshima N. 1980. On the equations of fully fluidized granular materials. *Z. Angew. Math. Phys.* 31:483–93
107. Windows-Yule CRK, Weinhart T, Parker DJ, Thornton AR. 2014. Influence of thermal convection on density segregation in a vibrated binary granular system. *Phys. Rev. E* 89:022202
108. Windows-Yule C, Rosato A, Parker DJ, Thornton AR. 2015. Maximizing energy transfer in vibrofluidized granular systems. *Phys. Rev. E* 91:052203
109. Windows-Yule C, Rosato A, Thornton A, Parker DJ. 2015. Resonance effects on the dynamics of dense granular beds: achieving optimal energy transfer in vibrated granular systems. *New J. Phys.* 17:023015
110. Wildman R, Huntley J. 2008. Experimental measurements and modelling of rapid granular flows. *Powder Technol.* 182:182–91
111. Wildman R, Martin T, Huntley J, Jenkins J, Viswanathan H, et al. 2008. Experimental investigation and kinetic-theory-based model of a rapid granular shear flow. *J. Fluid Mech.* 602:63–79
112. Wildman R, Parker DJ. 2002. Coexistence of two granular temperatures in binary vibrofluidized beds. *Phys. Rev. Lett.* 88:064301
113. Ottino JM, Khakhar D. 2000. Mixing and segregation of granular materials. *Annu. Rev. Fluid Mech.* 32:55–91
114. Ahmad K, Smalley I. 1973. Observation of particle segregation in vibrated granular systems. *Powder Technol.* 8:69–75
115. Khakhar D, McCarthy J, Ottino JM. 1997. Radial segregation of granular mixtures in rotating cylinders. *Phys. Fluids* 9:3600–14
116. Tunuguntla DR, Bokhove O, Thornton AR. 2014. A mixture theory for size and density segregation in shallow granular free-surface flows. *J. Fluid Mech.* 749:99–112
117. Rosato AD, Blackmore DL, Zhang N, Lan Y. 2002. A perspective on vibration-induced size segregation of granular materials. *Chem. Eng. Sci.* 57:265–75
118. Arntz M, den Otter WK, Briels WJ, Bussmann P, Beeftink H, Boom R. 2008. Granular mixing and segregation in a horizontal rotating drum: a simulation study on the impact of rotational speed and fill level. *AIChE J.* 54:3133–46

119. Feitosa K, Menon N. 2002. Breakdown of energy equipartition in a 2D binary vibrated granular gas. *Phys. Rev. Lett.* 88:198301
120. Windows-Yule K, Parker DJ. 2015. Density-driven segregation in binary and ternary granular systems. *KONA Powder Part. J.* 32:163–75
121. Windows-Yule C, Parker DJ. 2014. Inelasticity-induced segregation: why it matters, when it matters. *Europhys. Lett.* 106:64003
122. Windows-Yule C, Parker DJ. 2014. Self-diffusion, local clustering and global segregation in binary granular systems: the role of system geometry. *Powder Technol.* 261:133–42
123. Windows-Yule C, Parker DJ. 2014. Center of mass scaling in three-dimensional binary granular systems. *Phys. Rev. E* 89:062206
124. Windows-Yule CRK, Moore A, Wellard C, Parker DJ, Seville JPK. 2020. Particle distributions in binary gas-fluidised beds: Shape matters—but not much. *Chem. Eng. Sci.* 216:115440
124a. Windows-Yule CRK, Gibson S, Parker DJ, Kokalova TZ, Seville JPK. 2020. Effect of distributor design on particle distribution in a binary fluidised bed. *Powder Technol.* 367:1–9
125. Hsiau SS, Chen C. 2000. Granular convection cells in a vertical shaker. *Powder Technol.* 111:210–17
126. Hsiau SS, Wang PC, Tai CH. 2002. Convection cells and segregation in a vibrated granular bed. *AIChE J.* 48:1430–38
127. Windows-Yule C, Parker DJ. 2014. Energy non-equipartition in strongly convective granular systems. *Eur. Phys. J. E* 37:17
128. Ingram A, Yang Z, Bakalis S, Parker DJ, Fan X, et al. 2007. Multiple particle tracking in a fluidised bed. *Proceedings of the 12th International Conference on Fluidization: New Horizons in Fluidization Engineering* (*Fluidization XII*), pp. 449–52. Brooklyn, NY: Eng. Conf. Int.